



# Electrochemical Sensors Based on Manganese and Cobalt Oxide Nanostructures for the Detection of Flutamide and its Derivatives in Real Water Samples

Thompho Ravele<sup>1</sup> · Ntuthuko W. Hlongwa<sup>1</sup> · Thabo T. I. Nkambule<sup>1</sup> · Nozipho N. Gumbi<sup>1</sup> · Kutloano E. Sekhosana<sup>1</sup>

Received: 20 April 2023 / Accepted: 4 July 2023 / Published online: 27 July 2023  
© The Author(s) 2023

## Abstract

Flutamide (FLU), bicalutamide (BIC), and hydroxyflutamide (OHF), having a low biodegradability, may cause severe health effects on humans as antiandrogens. In this work, we have developed two electrochemical sensors using manganese oxide ( $\text{MnO}$ ) and Cobalt oxide ( $\text{CoO}$ ) nanostructures (NSs) as electrocatalysts. The GCE modified with  $\text{MnO}$  is referred to as  $\text{MnO}/\text{GCE}$  and the GCE modified by  $\text{CoO}$  is referred to as  $\text{CoO}/\text{GCE}$ . The electrochemical behaviours of  $\text{CoO}/\text{GCE}$  and  $\text{MnO}/\text{GCE}$  were examined in ferricyanide solution. It was observed through the employment of cyclic voltammetry that  $\text{MnO}/\text{GCE}$  exhibit better electron transfer than  $\text{CoO}/\text{GCE}$ . The calculated surface coverage values,  $1.46 \times 10^{-9} \text{ mol cm}^{-2}$  and  $5.02 \times 10^{-9} \text{ mol cm}^{-2}$  of  $\text{MnO}/\text{GCE}$  and  $\text{CoO}/\text{GCE}$  suggest a multilayer of a metal oxide molecule film at the surfaces of glassy carbon electrodes (GCE). FLU, BIC and OHF were detected at a linear range from 32.01 to 50.00  $\mu\text{M}$ . The limits of detection of FLU, BIC and OHF were 18.5, 13.0 and 78.8  $\mu\text{M}$  at  $\text{MnO}/\text{GCE}$  respectively and 18.8, 18.7 and 18.5  $\mu\text{M}$  at  $\text{CoO}/\text{GCE}$  respectively. Both  $\text{MnO}/\text{GCE}$  and  $\text{CoO}/\text{GCE}$  showed good catalytic stability towards detecting FLU and its derivatives. FLU, BIC and OHF were also detected in the presence of interferents for both electrochemical sensors in phosphate buffer solution. Both  $\text{MnO}/\text{GCE}$  and  $\text{CoO}/\text{GCE}$  confirmed good selectivity without cross interference. Some of the health effects associated with FLU, BIC and OHF are liver damage, prostate inflammation, and methamoglobinemia. Although FLU, BIC and OHF are detected in low concentration levels in water bodies, their continuous ingestion is a great concern. As far as we know,  $\text{MnO}$  and  $\text{CoO}$  NSs have not been used to electrochemically detect FLU, BIC and OHF. Furthermore, OHF has not been detected electrochemically before and there are only a few studies on the electrochemical detection of BIC. Hence,  $\text{MnO}$  and  $\text{CoO}$  NSs are used in this study for the first time for an electrochemical sensor fabrication towards the detection of FLU, BIC and OHF.

**Keywords** Flutamide · Bicalutamide · Hydroxyflutamide · Metal oxide nanostructures · Electrochemical sensor

## Introduction

Metal oxide nanomaterials (MONMs) have been widely explored in research due to their structural diversity and exceptional physicochemical properties [1, 2]. MONMs have been employed for applications in catalysis [3, 4], water treatment [5, 6], wettability [7, 8], Li-ion batteries [9, 10]

as well as electrochemical sensing [11, 12]. Among them, manganese oxide nanomaterials (MnONMs) have attracted a lot of interest due to their low cost, environmental benignity, high specific surface area, good electrocatalytic activity, good stability, crystal structure, defect chemistry, morphology, textures as well as selective ability [13–18]. The existence of MnOMNs in different forms of stable oxide and crystal structures like  $\text{MnO}$ ,  $\text{MnO}_2$ ,  $\text{Mn}_2\text{O}_3$ , and  $\text{Mn}_3\text{O}_4$  is one of their interesting properties [19]. Another interesting metal oxide is cobalt oxide due to their excellent properties., cobalt oxide nanostructures are gaining attention because of their electrocatalytic properties, low cost, environmental friendliness, excellent conductivity and chemical stability [20–23]. The transformation of  $\text{Co}^{2+}$  or  $\text{Co}^{3+}$  brings about high absorption of oxygen contents as well as distinctively

✉ Kutloano E. Sekhosana  
sekhone@unisa.ac.za

<sup>1</sup> Institute for Nanotechnology and Water Sustainability (iNanoWS), College of Science, Engineering and Technology (CSET), University of South Africa, Cnr Christiaan De Wet and Pioneer Avenue, Roodepoort 1709, Florida, South Africa

surface reactivity on the surface of the material. Consequently, cobalt oxide nanomaterials (CoOMNs) provide excellent performance in many fields, such as pigments, electrochemistry and catalysis [24].

MONMs have been employed in the electrochemical detection of emerging pollutants; including AAs with side effects such as sleeping disorders, skin reactions, liver malfunction, anaemia, headache, dizziness, blurred vision, depression, nausea, Jaundice, and reduction of white blood cells and blood platelets [25–29]. Due to the side effects of AAs seemingly overshadowing their efficacy, there is a need to develop a method to determine these compounds. Comparison of analytical methods that have been employed to determine and control FLU, BIC and OHF have been executed and prove that electrochemistry is the most reliable method [30–32].

Electrochemical sensors have interesting properties such as high sensitivity, fast response time, low cost, simplicity, possibility of miniaturization as well as integration in portable devices [33–36]. Additionally, electrochemical sensors have a capability of detecting a wide range of compounds such as organic, inorganic, ionic or neutral molecules as well as metal ions [37–39]. The combination of these fascinating properties of electrochemical sensors with those of metal oxide nanoparticles has resulted in powerful electrochemical sensing platforms.

Various materials such as LNW/CPE [40], CuO/GO/PANI [41], ZnO-Co<sub>3</sub>O<sub>4</sub>@C<sub>3</sub>N<sub>4</sub> NC [33], ZnMn<sub>2</sub>O<sub>4</sub>-PGO [42] and sCu<sub>2</sub>V<sub>2</sub>O<sub>7</sub>/S-rGO [43] nanocomposites have been employed as electrocatalysts for the determination of AAs. However, these materials have some limitations such as low sensitivity, high cost of precursor as well as use of separate instruments for synthesis [18]. In this study cobalt oxide and manganese oxide nanostructures (NSs) will be our material choice for an electrochemical sensor fabrication towards the detection of FLU. This is because metal oxide NSs possess superior electrochemical properties and, thus, have been employed as electrocatalytic and energy storage materials [44–46]. To the best of our knowledge, cobalt oxide and manganese oxide NSs have not been used to electrochemically detect AAs. Hence, these NSs are used in this study for the first time for an electrochemical sensor fabrication towards the detection of FLU, BIC and OHF.

## Experimental Section

### Materials Used

Manganese (II) chloride (99%), cobaltous chloride anhydrous (98%), potassium chloride boixtra (99%), potassium ferricyanide (III) (K<sub>3</sub>Fe<sub>3</sub>(CN)<sub>6</sub>, 99%), potassium hexacyano-ferrate (II) trihydrate (K<sub>4</sub>Fe(CN)<sub>6</sub>, 98.5–102.0%), FLU(<=

100%), (OHF (98%) and BIC (98%) were purchased from Sigma-Aldrich. Sodium hydroxide (98%) and hydrochloric acid were purchased from Merck. All chemicals used in this study were of analytical grade and all solutions were prepared with milliQ Water.

## Synthesis

### Synthesis of Manganese Oxide NSs

Manganese oxide NSs were prepared according to literature [47] with minor modifications as follows. Manganese (II) chloride (1 g, 0.0080 mmol) was dissolved in milli-Q water (30 mL) and sonicated for 20 min. To adjust the pH, drops of sodium hydroxide (2 M) were added to the solution until the pH was 9. The mixture was sonicated and transferred to a stainless-steel autoclave (50 mL) and placed in an oven heated at 160 °C for 18 h. The reaction mixture was cooled naturally to room temperature before being centrifuged and washed two times with methanol. The product was dried in oven heated at 60 °C.

### Synthesis of Cobalt Oxide NSs

Cobalt oxide NSs were synthesised according to a method reported elsewhere, [47] with minor modifications as follows. Cobaltous chloride anhydrous (1 g, 0.0077) was dissolved in milli-Q water (30 mL). Drops of sodium hydroxide solution (2 M) were added to the solution to adjust the pH to 9. The mixture was then sonicated and transferred to a stainless-steel autoclave (50 mL) and heated in an oven at 160 °C for 18 hours. The reaction mixture was then cooled to room temperature, centrifuged, and washed with methanol. The product was dried in an oven at 60 °C.

## Characterization Techniques

Milli-Q water was obtained from Milli-Q® Reference Water Purification System from Merck. pH was measured using a pH meter from Lasec. Infrared spectra were recorded on a Perkin Elmer FT-IR spectrometer frontier (FTIR). Ultra-violet–Visible spectra (UV–Vis) were recorded on a PerkinElmer Lambda 60 UV–Vis spectrophotometer. The morphology of the as-prepared materials was examined using scanning electron microscope (SEM-JEOL) (Japan) and transmission electron microscope (TEM). Energy dispersive X-ray spectra (EDS) were obtained using a SEM-JOEL (Japan) equipped with oxford (UK) EDS. The voltammetric measurements were performed using PalmSens EmStat4M potentiostat using PTrace software for windows. Conventional three-electrode system employing a GCE (unmodified and modified) as a working electrode, platinum plate as a

counter electrode and Ag/AgCl (saturated KCL) as a reference electrode was used for electrochemical studies.

### Fabrication of Metal Oxide Nanostructure Modified GCE

The metal oxide (MnO and CoO) nanostructure-based electrochemical sensors were developed according to the following steps. Firstly, GCE was cleaned using 0.3 µm alumina slurry and subjected to sonication (10 min) in ethanol. The polished GCE surface was then dried at room temperature. Thereafter, the as-prepared metal oxide NSs (2 mg) were dissolved in dimethylformamide (DMF) and sonicated for 20 min to get homogeneous metal oxide NSs solutions. Solutions of metal oxide NSs (10 µL) were then drop casted on the GCE surface and allowed to dry in the oven at 60 °C. The obtained metal oxide NSs modified GCE surfaces were gently rinsed with DI water to remove loosely attached molecules on the GCE surface. The obtained MnO/GCE and CoO/GCE were employed for further electrochemical experiments.

### Real Sample Analysis

Tap water, obtained from synthesis laboratories at the University of South Africa, was used as real samples. The tap water was treated using NaH<sub>2</sub>PO<sub>4</sub>, Na<sub>2</sub>HPO<sub>4</sub> and HCl and the pH was adjusted to pH 5.

## Results and Discussion

### FTIR and UV–Vis Analysis

The functional groups of the bonding entities on the as-prepared materials were studied using FTIR analysis. The FTIR spectrum shown at Fig. S1A for MnO NSs shows the absorption peak around 1160 and 1099 cm<sup>-1</sup> which can be linked to O–Mn–O and Mn stretching vibration, respectively. Similar results were reported by Moon et al [48]. The spectrum proves the formation from the metal oxide (MO) NSs from the metal salts used in the synthesis. Fig. S1B represents the FTIR spectrum of CoO NSs and shows peaks around 650, 750 and 840 cm<sup>-1</sup> which can be attributed to Co–O and O–Co–O stretching. The broad peak observed around 1620 cm<sup>-1</sup> can be attributed to O–H stretching. These wavenumbers are closer to the wavenumbers of NPs reported in literature [49, 50]. The spectra clearly prove the formation from the metal oxide (MO) NSs. UV–Vis technique was employed to study the ground state electronic absorption of the as-prepared nanomaterials. Fig. S1C shows the UV–Vis spectrum of MnO NSs, which have a wide absorption band at 300–606 nm with the absorption peak at 400 nm. The

absorption peak of MnO NSs was absorbed at the same region as other MnO NPs [51, 52]. The UV–Vis spectrum of CoO NSs is shown in Fig. S1D with an absorption peak at 450 nm. Other CoO NPs also showed the same shape and absorption peaks at 280 and 400 nm which is in close proximity to what was observed for CoO NSs [53].

### Surface Morphology

#### SEM Analysis

The surface morphologies of the as-prepared MnO NSs and CoO NSs were examined using SEM. Fig. S2A shows the SEM image of the as-prepared MnO NSs that were synthesized by the hydrothermal reaction. The image shows a big nest-like nanostructure which seem to exhibit a porous structure. Furthermore, the formation of the nest-like morphology was comprised of small rod-like petals of uniform particle size distribution. The SEM image of MnO NSs resemble that of other MnO NSs as previously reported in literature [54–56]. Fig. S2B shows SEM image of CoO NSs. From the figure, small-clustered structures were observed, with some coming together to form a bigger cluster. The nanostructures had uniform particle size distribution with one agglomerate. The small clustered CoO NSs resemble those of CoO NSs reported in literature [57–59]. The SEM images prove the successful formation of MnO and CoO NSs respectively.

#### EDX Analysis

**EDX Analysis of MnO and CoO NSs** EDX analysis was also employed for the detection of elemental composition of the as-prepared materials. Fig. 1A displays the EDX spectrum of MnO NSs. The EDX spectrum confirms the presence of carbon, oxygen and manganese elements only, thereby endorsing the purity and distinct formation of MO (MnO) NSs. The spectrum emitted prominent peak in the manganese region which strongly indicates the presence of manganese, corresponding to 73.3 mass% of manganese. Another peak was that of oxygen which corresponded to 36.2 mass% of oxygen. The mass percentages are in correspondence to the synthetic content of MnONNs as there was more manganese used than the source of oxygen where only drops were used in the synthesis. As shown in Fig. 1B, the presence of cobalt, oxygen and carbon was confirmed as well as the presence of chlorine element which comes from the manganese chloride precursor used in the hydrothermal synthesis of CoO NSs. These detection of these elements prove the formation of CoO NSs. The spectrum shows a prominent peak in the cobalt region which corresponds to 67 mass% of cobalt. The other peaks observed are those of oxygen and chlorine corresponding to 24.6 mass% and 8.4 mass%, respectively. The mass percentages correspond to the syn-

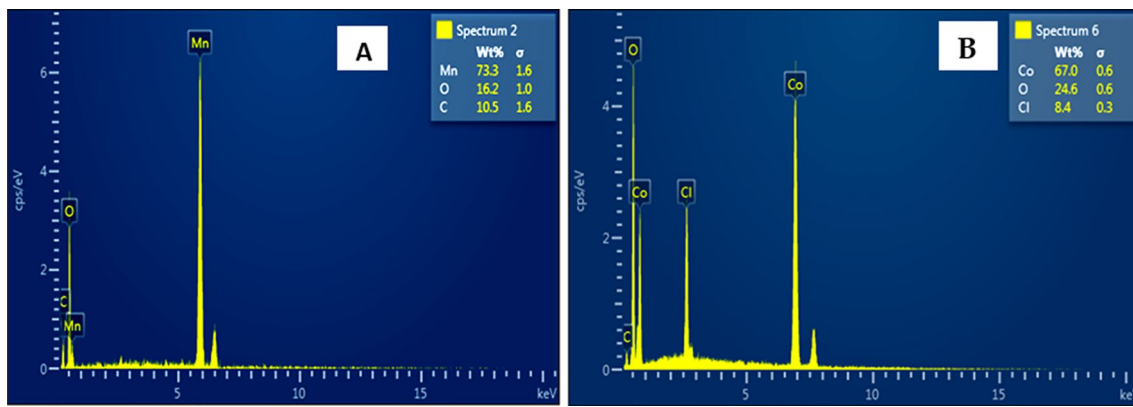


**Fig. 1** EDX spectra of **A** MnO NSs and **B** CoO NSs

thesis method used as cobalt was in the precursor dissolved and the only source of oxygen was the drops added to the solution with chlorine being an impurity from the precursor.

**EDX mapping of MnO and CoO NSs** The elemental mapping of MnO NSs was also employed in this study using EDX and it is shown in Fig. 2. Figure 2A displays the elemental mapping of the mixture of elements on the surface of MnO NSs. The mapping images further reveal the presence of manganese, oxygen and carbon elements in their respective elemental mapping depicted in Fig. 2B–D respectively. The carbon observed is due to the carbon tape used during analysis. The Elemental mapping of CoO NSs was also taken. Fig. 2E displays the mapping of the mixture of elements on the surface of CoO NSs as displayed. The mapping images further reveal the presence of cobalt, oxygen, carbon which can be attributed to the carbon tape and chlorine which is result of the cobalt chloride precursor used as depicted in their respective elemental mapping denoted by Fig. 2F–I, respectively. The presence of the elements in Fig. 2 further proved the purity and presence of the appropriate elements at the surface of the as-prepared NSs.

#### TEM Analysis of MnO and CoO NSs

The surface morphologies of the as-prepared materials were further examined using TEM analysis. The TEM image of MnO NSs is displayed in Fig. S3A shows uniform size particles with morphologies of rods coming together to form clusters with some nearly spherical particles on the side. Fig. S3B shows the TEM image of the as-prepared CoO NSs. The image shows small rod-like structures clusters of non-uniform particle size distribution.

#### XRD Analysis of MnO and CoO NSs

The x-ray patterns of as-prepared materials shown in Fig. S4 were evaluated using XRD technique as. The x-ray diffractograms of MnO NSs are shown in Fig. S4A and revealed pure phase of MnO NSs and all the diffraction peaks could be indexed to (JCPDS No. 88-0649) determining  $\gamma$ -MnOOH of the tetragonal symmetry [60, 61]. The observed diffraction peaks of MnO NSs are (111), (020), (111), (002), (121), (210), (220), (222), (113), (131), (131), (202) and (131). The prominent diffraction peak at  $2\theta = 26.1$  (111) demonstrates excellent crystalline quality of MnO NSs. Fig. S4B shows the x-ray diffractograms of CoO NSs evaluated by XRD. The diffraction peaks in the spectrum depicts a pure phase of CoO NSs and could be indexed to (JCPDS No. 43-1003) of the cubic symmetry [62]. The observed diffraction peaks of CoO NSs are (111), (220), (311), (222), (400), (511), and (440). The prominent diffraction peak at  $2\theta = 36.8$  (311) demonstrates excellent crystalline quality of CoO NSs.

#### Electrochemical Sensing

##### Characterization of the Fabricated Electrochemical Sensors by Cyclic Voltammetry

Characterization of the modified electrodes was achieved through cyclic voltammetry (CV) in a solution consisting of  $K_3Fe_3(CN)_6$  (1 mM),  $K_4Fe(CN)_6$  (1 mM) and KCl (0.1 M) in which the cyclic voltammograms of the unmodified GCE (Bare GCE) and the modified GCE (MnO/GCE and CoO/GCE) were measured (Fig. 3A and Fig. S5A). The resultant voltammograms were used to monitor the electron transfer efficiency in terms of peak-to-peak separation ( $\Delta E_p$ ). The lowest  $\Delta E_p$  value (0.22 V) indicates better electron transfer. MnO/GCE (0.22 V) had a better electron transfer, followed by CoO/GCE (0.25 V). Lower electron transfer suggest hindrance on the surface of the electrode due to the adsorption

**Fig. 2** EDX mapping of **A** mixture of elements; **B** Manganese; **C** Oxygen; **D** Carbon; **E** mixture of elements; **F** Cobalt; **G** Oxygen; **H** Carbon; **I** Chlorine

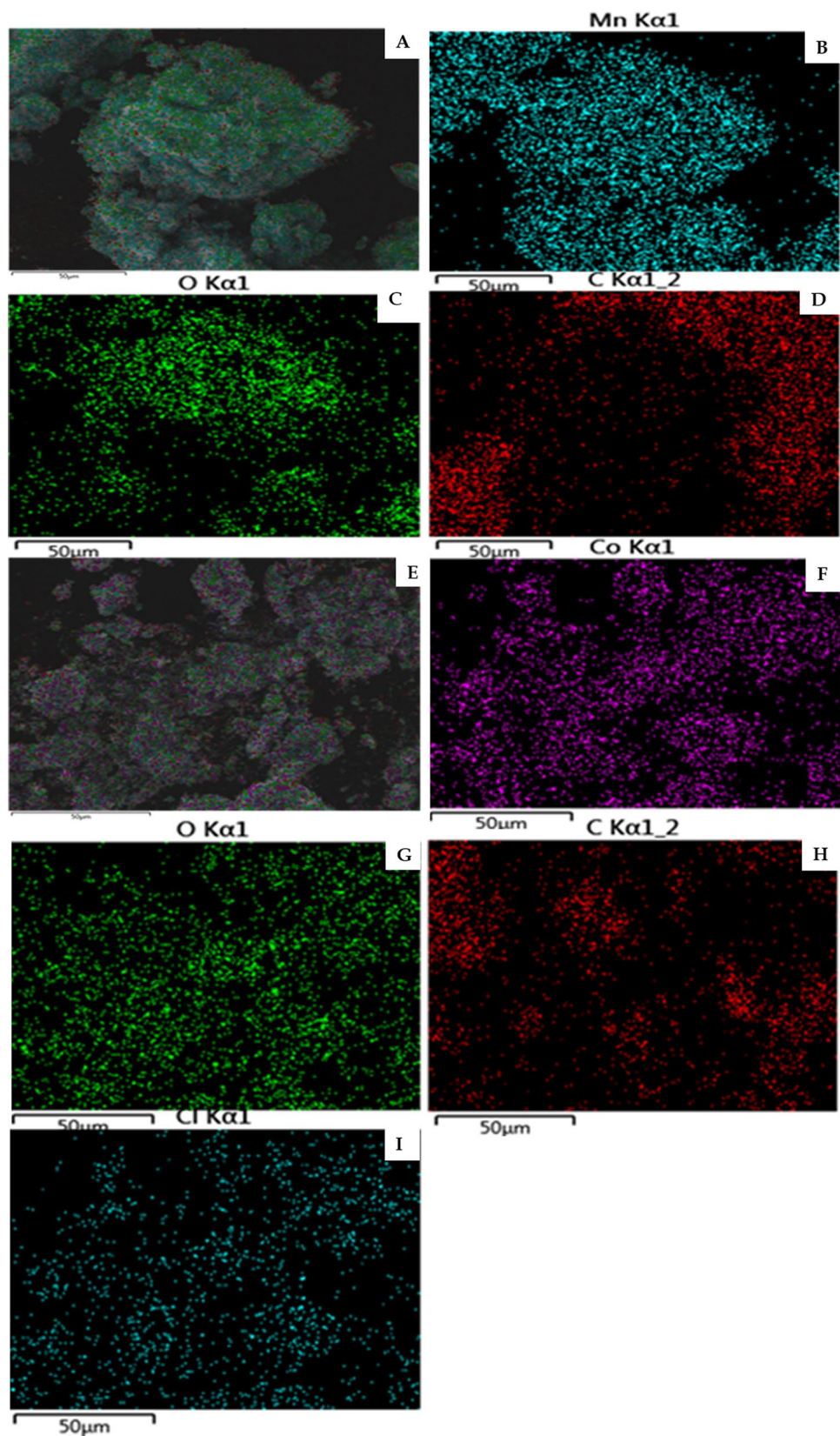
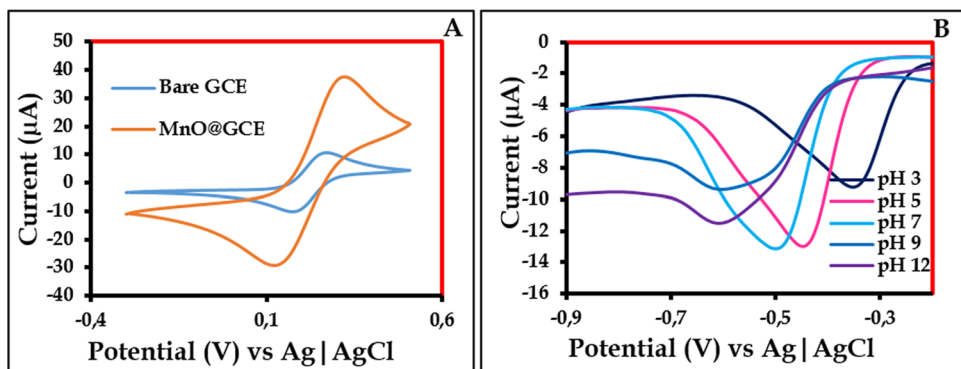


**Fig. 3** **A** Cyclic voltammograms of bare GCE in comparison to MnO/GCE in ferricyanide solution; **B** Square Wave voltammograms for 1 mM FLU on the surface of MnO/GCE in PBS at pH 3, pH 5, pH 7, pH 9 and pH 12



of the electrocatalyst material [63]. Surface roughness of the modified electrode is among the most important factors contributing to the differences in  $\Delta E_p$  values [64]. Consequently, Eq. 1 which reflects the Randles-Sevcik relationship for reversible systems was applied on  $K_3Fe_3(CN)_6/K_4Fe(CN)_6$  redox system to determine the surface roughness factors of modified electrodes [65].

$$I_p = 2.69 \times 10^5 n^{\frac{3}{2}} ACD^{\frac{1}{2}} v^{\frac{1}{2}} \quad (1)$$

Where  $n$  is the number of electrons involved in the redox reaction,  $A$  is the surface area of the electrode ( $\text{cm}^2$ ),  $D$  is the diffusion coefficient of the molecule in the bulk solution,  $C$  is the concentration of the molecule in the bulk solution ( $\text{M}$ ), and  $V$  is the scan rate ( $\text{V.s}$ ). The  $D$  value for  $K_3Fe_3(CN)_6/K_4Fe(CN)_6$  system has been reported as  $7.6 \times 10^{-6} \text{ cm}^2 \text{ s}^{-1}$  [65]. The scan rate used in these experiments was  $100 \text{ mVs}^{-1}$  and while  $n$  was assumed to be 1. The theoretical  $I_p$  was calculated to determine the surface roughness factors of the modified electrodes, defined as the experimental  $I_p$ /theoretical  $I_p$  ratio. The corresponding real electrode areas [definition: roughness factor  $\times$  theoretical surface area ( $0.071 \text{ cm}^2$ )] were used to calculate surface coverage  $\Gamma$  ( $\text{mol cm}^{-2}$ ) for each modified GCE using Eq. 2 [66].

$$\Gamma = \frac{Q}{nFA} \quad (2)$$

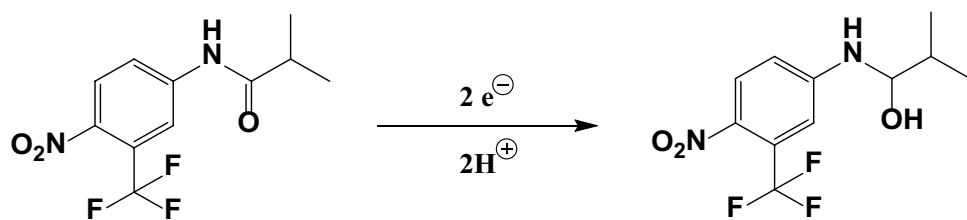
where  $Q$  is the charge,  $n$  is the number of electrons involved,  $F$  is the Faraday constant ( $96\,485 \text{ C mol}^{-1}$ ),  $A$  is the surface area of the electrode. The  $\Gamma$  values for modified electrodes less than  $1 \times 10^{-10} \text{ mol cm}^{-2}$  are reported to imply

a monolayer molecule film of the material on the electrode surface [66]. The  $\Gamma$  values for the electrodes modified with metal oxide NSs are greater than  $1 \times 10^{-10} \text{ mol cm}^{-2}$  and increase in the following order: CoO/GCE < MnO/GCE. These  $\Gamma$  values for MnO/GCE ( $1.46 \times 10^{-9} \text{ mol cm}^{-2}$ ) and CoO/GCE ( $5.02 \times 10^{-9} \text{ mol cm}^{-2}$ ) suggest a multilayer of a metal oxide molecule film on the electrode surface [67].

#### Optimization of Experimental Parameters for Electrochemical Sensing

In order to determine the working conditions, square wave voltammetry (SWV) was employed to study the effects of pH of the buffer solutions. This is because the pH of the electrolyte solution has a significant influence on the electrochemical process of any electroactive molecule on the surface of the electrode. The influence of pH was investigated in 1 mM FLU electrolyte solutions (PBS) at pH 3, pH 5, pH 7, pH 9 and pH 12 to establish which pH was best suitable for studying the solutions of FLU, BIC and OHF. Fig. 3B shows a better response in peak current for pH 5 and pH 7 at MnO/GCE in comparison to those observed at pH 3, pH 9 and pH 12. pH studies were repeated for CoO/GCE to establish the suitable condition between pH 5 and pH 7 (Fig. S5B). CoO/GCE was behaving better at pH 5 than at pH 7. The sensors showing higher peak current response at pH 5 maybe due to the hydrogen ion as the hydrogen ion is said to play an important role in the reduction process. A higher peak current response is expected at acidic conditions for reduction processes. The detailed mechanism of the reduction of FLU is shown in Scheme 1 and it further reveals the importance

**Scheme 1** mechanism of the reduction of FLU



of the hydrogen ion in the reduction process of FLU. The pKa value of the developed sensors with respect to FLU detection was calculated to be 5. Thus pH 5 was employed as the optimum pH for further studies.

### Influence of Scan Rate

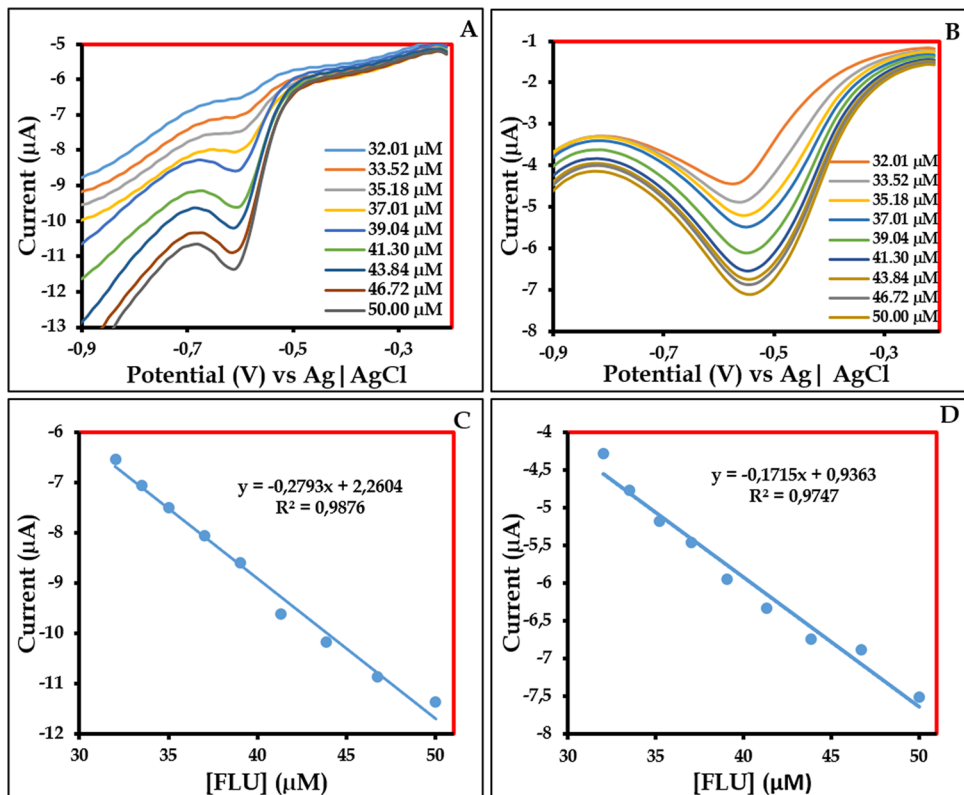
The influence of scan rate on the electrochemical reduction performances of FLU, BIC and OHF on MnO/GCE and CoO/GCE was studied using CV. The scan rate studies were performed at a constant concentration of 1 mM in PBS (pH 5) from 10 mV/s to 100 mV/s. Fig. S6A and B show changes in the cathodic peak current with the increase in the scan rates for MnO/GCE and CoO/GCE together with their corresponding linear relationship plots (Fig. S6C and D), respectively for FLU. Similarly, Fig. S6 shows the catalytic behaviour of (C) BIC at MnO/GCE and (D) BIC at CoO/GCE showing the (E) OHF at MnO/GCE and (F) OHF at CoO/GCE with their corresponding linear relationships (Fig. S6 G, H, I, J, K and L), respectively. Fig. S6A shows a reduction process occurring at each scan for FLU. The peaks at  $-0.870$  V depicts the direct reduction of FLU to hydroxylamine and has no catalytic anodic current peak observed. The cathodic peak represented the reduction of nitroso derivative to hydroxylamine derivatives [68]. The linear relationships are expressed as plots of the peak currents vs. the square roots of the scan rates. As shown in Fig.

S6A–F, the cathodic peak currents continuously increased as the scan rate increased for all analytes. As can be observed in Fig. S6G–L, the peak currents are linearly proportional to the square roots of scan rates. The correlation coefficients ( $R^2$ ) were 0.9931 and 0.9899 for the reduction processes of FLU at MnO/GCE and CoO/GCE respectively (Fig. S10G and H). For BIC,  $R^2$  values were 0.9834 and 0.9914 for the irreversible reduction process as shown in Fig. S10I and J. As depicted in Fig. S10K and L, the  $R^2$  values were 0.9978 and 0.9853 for the reduction process of OHF. This linear relationships denote diffusion-controlled processes on the surfaces of modified electrodes [69]. The diffusion-controlled electrode reactions occur if the spontaneous transfer of the electroactive species is from regions of higher concentrations to regions of lower concentrations. This is seen by a directly proportional between current and the square root of scan rate. Most electrode reaction reported in literature are diffusion-controlled [70–72].

### Concentration Studies

Concentration studies were performed to investigate the electrochemical performance of MnO/GCE and CoO/GCE towards detecting and quantifying FLU, BIC and OHF using square wave voltammetry (SWV). Fig. 4 and Fig. S7 shows the response of MnO/GCE and CoO/GCE when varying concentration. Concentration variations of each analyte

**Fig. 4** SWVs of FLU at **A** MnO/GCE and **B** CoO/GCE at different concentrations (32.01–50.00  $\mu$ M) and their corresponding linear relationship plots (C and D) for MnO/GCE



were analysed to establish the electrolytical parameters such as limit of detections (LODs) and limit of quantifications (LOQs). Analysis was performed at concentration ranges from 32.01 to 50.00  $\mu\text{M}$  in PBS (pH 5) at a scan rate of 100 mV/s with serial dilutions performed from 50 to 32.01  $\mu\text{M}$ . Fig. 4A and B represents the behaviour of MnO/GCE and CoO/GCE towards the detection of FLU. As can be seen, the increase in concentration of FLU resulted in an increase in the reduction peak current (Fig. S7A and B). The resultant peak currents were plotted against concentration to obtain a linear relationship plot as shown in Fig. 4C and D, respectively. The same behaviour was observed in Fig. S7 for the detection of (A) BIC at MnO/GCE, (B) BIC at CoO/GCE, (C) OHF at MnO/GCE and (D) OHF at CoO/GCE with their resultant linear relationships of Concentration vs peak current (Fig. S7E, F, G and H), respectively. The linear relationship plots were then used to calculate the LODs and LOQs of MnO/GCE and CoO/GCE (estimated from  $= 3 \frac{SD}{B}$ ). For the MnO/GCE electrode sensor, the LODs of FLU, BIC and OHF are 18.5, 13.0 and 78.8  $\mu\text{M}$ . The LOQs (estimated using  $LOQ = 10 \frac{SD}{B}$ ) for FLU, BIC and OHF are 81.8, 43.2 and 25.8  $\mu\text{M}$ . For the CoO/GCE electrode sensor, the LODs of FLU, BIC and OHF are 18.8  $\mu\text{M}$ , 18.7  $\mu\text{M}$  and 18.5  $\mu\text{M}$  respectively. In addition, the LOQs of FLU, BIC and OHF are 82.0  $\mu\text{M}$ , 81.8  $\mu\text{M}$  and 81.8  $\mu\text{M}$  respectively. The LODs show the sensitivity of the study and are comparable with those reported in literature as provided in Table 1.

## Stability Studies

Stability of MnO/GCE and CoO/GCE for FLU, BIC and OHF were tested by running several scans at a fixed scan rate of 100 mV/s in FLU (1 mM), BIC (1 mM) and OHF (1 mM) in PBS. The obtained CVs shown in Fig. S8A and B are for the detection of FLU at MnO/GCE and CoO/GCE respectively and the CVs in Fig. S8 represent the detection of (C) BIC at MnO/GCE and (D) BIC at CoO/GCE,

(E) OHF at MnO/GCE and (F) OHF at CoO/GCE. The cathodic peak currents were observed at 0.6 V (FLU) and 0.7 V (BIC and OHF) at MnO/GCE. The cathodic peak currents were observed at 0.57 V (FLU), 0.85 V (BIC) and 0.8 V (OHF) at CoO/GCE. As can be observed from Fig. S8, both the cathodic peak currents and potentials remain almost unchanged. Thus, it can be concluded that both MnO/GCE and CoO/GCE are stable in all electrolyte solutions. Metal oxides accelerate the electron transfer through a number of processes such as electropolymerization, physical adsorption, covalent bonding or electrodeposition techniques [11, 75]. MnO and CoO NSs being transition metals bear multiple valences of metal ions which flip-flop between their valence states. As a result, MnO and CoO NSs are strong electrocatalysts for the electroreduction of FLU, BIC and OHF in alkaline solutions as the functional groups of these analytes undergo reduction through high/low valence states of MnO and CoO NSs [36]. Therefore, due to the covalent bond of the valence electrons, there is no electrode fouling. As a result, the MnO and CoO NSs show good stability as CVs show no change after many cycles.

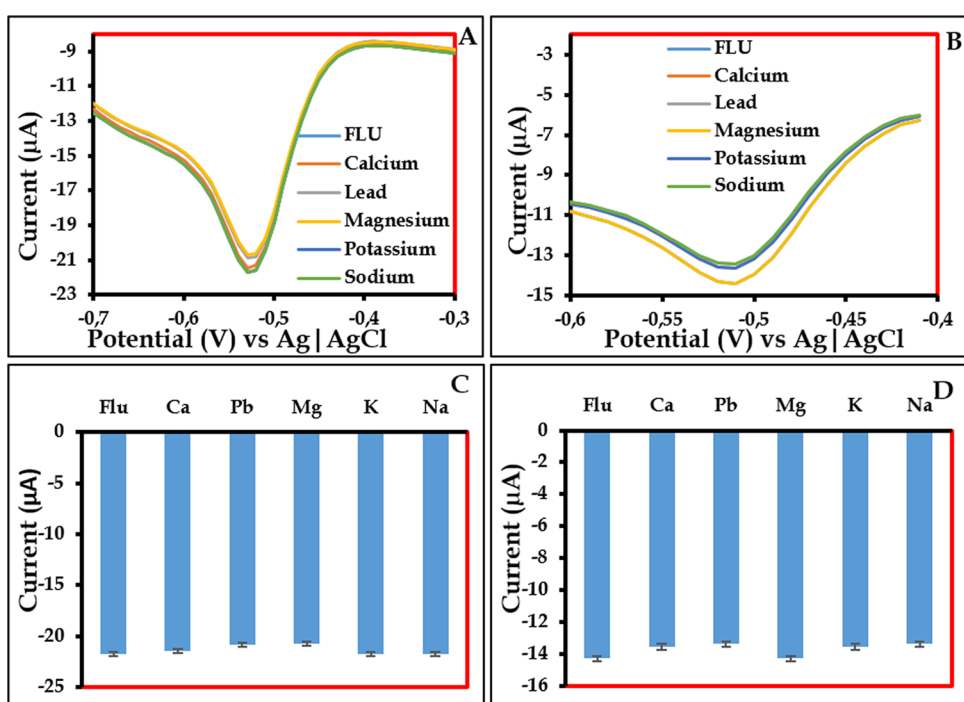
## Interference Studies

Square wave voltammetry was used to study the selectivity of MnO/GCE and CoO/GCE for FLU, BIC and OHF in the presence of different interferents. Interfering agents used in this study are  $\text{Ca}^+$ ,  $\text{Pb}^{2+}$ ,  $\text{Mg}^{2+}$ ,  $\text{K}^+$  as well as  $\text{Na}^+$ . The effect of these interferences were studied at 1 mM solutions of FLU, BIC and OHF and 1 mM of each interferent respectively. As can be seen in Fig. 5A and B; Fig. S9A–D, the interfering species did not affect the potential of the peak currents. The interfering species also did not affect the peak current intensity as the peaks are almost of the same current. The bar graphs and error bars in Fig. 5C and D; Fig. S9E–H also show that the change in peak current is very minimal. Thus, the inferring species do not interfere with

**Table 1** Comparison of limits of detection for determination of FLU, BIC and OHF at different electrodes

| Analyte | Modified electrode          | Limit of detection ( $\mu\text{M}$ ) | Linearity range ( $\mu\text{M}$ ) | References |
|---------|-----------------------------|--------------------------------------|-----------------------------------|------------|
| FLU     | nano-Ag/MGCE                | 9.33                                 | 10–1000                           | [31]       |
|         | AuE                         | 1.8                                  | 6–60                              | [23]       |
|         | BDDE                        | 0.42                                 | 0.99–42.9                         | [28]       |
|         | MnO/GCE                     | 18.5                                 | 32.01–50.00                       | This work  |
|         | CoO/GCE                     | 18.8                                 | 32.01–50.00                       | This work  |
|         | SWCNT/CPE                   | 0.005                                | 0.01–1                            | [73]       |
| BIC     | SrMoO <sub>4</sub> -MRs/GCE | 0.0012                               | 0.01–304.8                        | [74]       |
|         | MnO/GCE                     | 13.0                                 | 32.01–50.00                       | This work  |
|         | CoO/GCE                     | 18.7                                 | 32.01–50.00                       | This work  |
| OHF     | MnO/GCE                     | 78.8                                 | 32.01–50.00                       | This work  |
|         | CoO/GCE                     | 18.5                                 | 32.01–50.00                       | This work  |

**Fig. 5** SWVs of FLU at **A** MnO/GCE and **B** CoO/GCE in the presence of interfering species and the corresponding bar graphs (**C**) and (**D**) respectively



the electrochemical sensing of FLU, BIC and OHF at MnO/GCE and CoO/GCE. The reason for the high detection peak associated with the concentration of FLU, BIC and OHF whereas other interfering species do not show significant reduction peaks is that the hydrogen ion is the one playing a vital role in the reduction processes as shown in Scheme 1, therefore, due to the repulsion between the hydrogen ion and the cations from the interfering species only the analytes are reduced. As a result, interferents capped with organics should be considered in future studies.

### Real Sample Analysis

Real water samples were sprinkled with solutions of FLU, BIC and OHF (1 mM; 10 μL) repeatedly. Using SWV, it was observed that modified GCE (Fig. S10) could detect the analytes as evidenced by the enhancement of the catalytic peak currents with an increase in concentration. In addition to this, standard solutions of the analytes were added to samples, with their SWV signatures registered for the establishment of recoveries (Table 2). Fig. S10 show the real sample analysis of the analytes of interest at a linear range of 1.40–9.82 μM, at pH 5 and scan rate of 100 mV/s at MnO/GCE and CoO/GCE. Fig. S10A and B show the SWVs of the real sample analysis of FLU at MnO/GCE and CoO/GCE, respectively. As can be seen, the current was increasing negatively with the increase of concentration of each analyte. The same behaviour was observed for the detection of BIC (Fig. S10C and D, respectively) and OHF (Fig. S10E and F, respectively). The behaviour observed in

SWVs is also evidenced by the calibration curves for MnO/GCE and CoO/GCE (Fig. S10G and H, respectively) towards FLU. Similarly, for MnO/GCE and CoO/GCE towards BIC (Fig. S10I and J, respectively) and OHF (Fig. S10K and L, correspondingly) the same behaviour was recorded. The obtained % recoveries were 95.09%, 99.29% and 100% for FLU, BIC and OHF, respectively, at MnO/GCE sensor. The obtained % recoveries were 95.21%, 98.87% and 100% for FLU, BIC and OHF, respectively, at CoO/GCE sensor. The RSD % values ranged from 1.58 to 4.89 % at MnO/GCE and 2.3–7.22 % at CoO/GCE. The recoveries show good accuracy and reliability of MnO/GCE and CoO/GCE in the detection of the FLU, BIC and OHF.

### Conclusion and Future Perspectives

The successful synthesis of MnO and CoO NSs was affirmed by FTIR, UV–Vis, EDX, TEM and XRD. The NSs were then used to develop two simple sensors for the detection and quantification of FLU, BIC and OHF (MnO/GCE and CoO/GCE). Both MnO/GCE and CoO/GCE showed excellent and efficient electrocatalytic activities through CV and SWV methods. The cyclic voltammetric measurements revealed that the diffusion-controlled process was taking place at MnO/GCE and CoO/GCE reduction signals. The two electrochemical sensors showed good selectivity, stability, reliability, repeatability and reproducibility. SWV procedures with optimized operating parameters, the LOD values for FLU were determined at micromolar concentration levels for all reduction

**Table 2** comparison of recoveries (%) of FLU, BIC and OHF

| Electrode   | Sample | FLU                            |                                  |                               |              | BIC     |                                |                                  |                               | OHF          |         |                                |                                  |                               |              |         |
|-------------|--------|--------------------------------|----------------------------------|-------------------------------|--------------|---------|--------------------------------|----------------------------------|-------------------------------|--------------|---------|--------------------------------|----------------------------------|-------------------------------|--------------|---------|
|             |        | Amount added ( $\mu\text{L}$ ) | Expected conc. ( $\mu\text{M}$ ) | Found conc. ( $\mu\text{M}$ ) | Recovery (%) | RSD (%) | Amount added ( $\mu\text{L}$ ) | Expected conc. ( $\mu\text{M}$ ) | Found conc. ( $\mu\text{M}$ ) | Recovery (%) | RSD (%) | Amount added ( $\mu\text{L}$ ) | Expected conc. ( $\mu\text{M}$ ) | Found conc. ( $\mu\text{M}$ ) | Recovery (%) | RSD (%) |
| MnO/<br>GCE | 1      | 10                             | 1.40                             | 1.33                          | 95.1         | 2.40    | 10                             | 1.40                             | 1.39                          | 99.29        | 4.89    | 10                             | 1.40                             | 1.40                          | 100          | 1.58    |
| CoO/GCE     | 1      | 10                             | 1.40                             | 1.33                          | 95.1         | 2.30    | 10                             | 1.40                             | 1.38                          | 98.87        | 7.22    | 10                             | 1.40                             | 1.40                          | 100          | 5.69    |

peaks (32.01–50.00  $\mu\text{M}$ ). The effect of interfering species such  $\text{Ca}^+$ ,  $\text{Pb}^{2+}$ ,  $\text{Mg}^{2+}$ ,  $\text{K}^+$  and  $\text{Na}$  was very minimal. Thus, the inferring species do not interfere with the electrochemical sensing of FLU, BIC and OHF at MnO/GCE and CoO/GCE. The percent recoveries for both MnO/GCE and CoO/GCE ranged from 95 to 100 % at MnO/GCE and CoO/GCE. The RSD % values ranged from 1.58 to 4.89 % at MnO/GCE and 5.69–23% at CoO/GCE. Based on the studies employed in this study, it can be concluded that MnO/GCE and CoO/GCE may represent a simple, low-cost and comfortable electrochemical tool for routine analysis in pharmaceutical and environmental monitoring of contaminants. The limitation of the study is that the developed electrode sensors cannot detect metal ions as they repel the electrocatalyst materials on the surface of the electrode. The future perspectives of the study are In-depth interference, broader range and selectivity analysis; biological samples analysis; as well as Sensor validation and rigorous testing.

**Supplementary Information** The online version contains supplementary material available at <https://doi.org/10.1007/s10876-023-02474-z>.

**Acknowledgements** The authors would like to express their gratitude to Institute for Nanotechnology and Water Sustainability (iNanoWS), College of Science, Engineering and Technology (CSET), University of South Africa, as well as Council of Scientific and Industrial Research (CSIR) for supporting this work.

**Author Contributions** TR: wrote the research paper. NWH: supervisor who provided guidance and assisted in the characterization of materials. TTIN: supervisor who helped in putting together the structure of the manuscript. NNG: supervisor who read and restructured the manuscript. KES: supervisor who helped in the methodology, characterization of materials, data interpretation and structuring of the manuscript.

**Funding** Open access funding provided by University of South Africa. This study was financially supported by Institute for Nanotechnology and Water Sustainability at the College of Science, Engineering and Technology at the University of South Africa.

**Data Availability** The data presented in this manuscript is new and has not published elsewhere. This data includes figures (plots and images), and tables.

## Declarations

**Conflict of interest** Authors declare no competing interests.

**Ethical Approval** The study was conducted strictly under the guidelines stipulated in the ethics certificate (#2021/CSET/SOS/050) issued by University of South Africa on 28 April 2021 following approval by Ethics committee under School of Science at College of Science, Engineering and Technology. In this study, no human or studies were conducted.

**Open Access** This article is licensed under a Creative Commons Attribution 4.0 International License, which permits use, sharing, adaptation, distribution and reproduction in any medium or format, as long as you give appropriate credit to the original author(s) and the source, provide a link to the Creative Commons licence, and indicate if changes were made. The images or other third party material in this article are

included in the article's Creative Commons licence, unless indicated otherwise in a credit line to the material. If material is not included in the article's Creative Commons licence and your intended use is not permitted by statutory regulation or exceeds the permitted use, you will need to obtain permission directly from the copyright holder. To view a copy of this licence, visit <http://creativecommons.org/licenses/by/4.0/>.

## References

- Sundar, G. Venkatachalam, and S. J. Kwon (2018). Biosynthesis of copper oxide (CuO) nanowires and their use for the electrochemical sensing of dopamine. *Nanomaterials*. <https://doi.org/10.3390/nano8100823>.
- Kuang, Q., Wang, X., Jiang, Z., Xie, Z., and L. Zheng (2014). High-energy-surface engineered metal oxide micro- and nanocrystallites and their applications. *Acc. Chem. Res.* **47**, 308–318. <https://doi.org/10.1021/ar400092x>.
- Oelerich, W., Klassen, T., and R. Bormann (2001). Metal oxides as catalysts for improved hydrogen sorption in nanocrystalline Mg-based materials. *J. Alloys Compd.* **315**, 237–242. [https://doi.org/10.1016/S0925-8388\(00\)01284-6](https://doi.org/10.1016/S0925-8388(00)01284-6).
- Lin, X., Zhang, Z., Zhang, J., Sun, Q., Wang, C., and U. Pittman (2018). Catalytic fast pyrolysis of a wood-plastic composite with metal oxides as catalysts. *Waste Manag.* **79**, 38–47. <https://doi.org/10.1016/j.wasman.2018.07.021>.
- Raizada, P., Soni, V., Kumar, A., Singh, P., Parwaz Khan, A.M., Asiri, V.K., Thakur, V.H., Nguyen, Surface defect engineering of metal oxides photocatalyst for energy application and water treatment, Elsevier Ltd, 2021. <https://doi.org/10.1016/j.jmat.2020.10.009>.
- Yang, S. Y., Vecitis, C. D., and H. Park (2019). Electrocatalytic water treatment using carbon nanotube filters modified with metal oxides. *Environ. Sci. Pollut. Res.* **26**, 1036–1043. <https://doi.org/10.1007/s11356-017-8495-6>.
- Becenen, N., and Ö. Altun (2018). Investigation of the wettability and washing, perspiration and rubbing fastness of denim fabric in the presence of some nano-metal oxides and nano-Ag. *J. Text. Inst.* **109**, 914–919. <https://doi.org/10.1080/00405000.2017.1385967>.
- Hendraningrat, L., and O. Torsæter (2015). Metal oxide-based nanoparticles: revealing their potential to enhance oil recovery in different wettability systems. *Appl. Nanosci.* **5**, 181–199. <https://doi.org/10.1007/s13204-014-0305-6>.
- Flores, E., Novák, P., and E. J. Berg (2018). In situ and Operando Raman spectroscopy of layered transition metal oxides for Li-ion battery cathodes. *Front. Energy Res.* **6**, 1–16. <https://doi.org/10.3389/fenrg.2018.00082>.
- Charles, N., Yu, Y., Giordano, R., Jung, F., Maglia, F., and Y. Shao-Horn (2020). Toward Establishing Electronic and Phononic Signatures of Reversible Lattice Oxygen Oxidation in Lithium Transition Metal Oxides for Li-Ion Batteries. *Chem. Mater.* **32**, 5502–5514. <https://doi.org/10.1021/acs.chemmater.0c00245>.
- George, J. M., Antony, A., and B. Mathew (2018). Metal oxide nanoparticles in electrochemical sensing and biosensing: a review. *Microchim. Acta* **185**, 686560. <https://doi.org/10.1007/s00604-018-2894-3>.
- Rassaei, L., Marken, F., Sillanpää, M., Amiri, M., Cirtiu, C. M., and M. Sillanpää (2011). Nanoparticles in electrochemical sensors for environmental monitoring, TrAC - Trends Anal. Chem. **30**, 1704–1715. <https://doi.org/10.1016/j.trac.2011.05.009>.
- Wang, Y., Wang, L., and Q. Zhuang (2019). A ratiometric electrochemical sensor for dopamine detection based on hierarchical manganese dioxide nanoflower/multiwalled carbon nanotube nanocomposite modified glassy carbon electrode. *J. Alloys Compd.* **802**, 326–334. <https://doi.org/10.1016/j.jallcom.2019.06.124>.
- Wang, M. Y., Zhu, W., Ma, L., Ma, J. J., Zhang, D. E., Zhang, Z. W., Tong, Z., and J. Chen (2016). Enhanced simultaneous detection of ractopamine and salbutamol - Via electrochemical-facial deposition of MnO<sub>2</sub> nanoflowers onto 3D RGO/Ni foam templates. *Biosens. Bioelectron.* **78**, 259–266. <https://doi.org/10.1016/j.bios.2015.11.062>.
- Li, L., Shao, Q., and X. Huang (2020). Amorphous Oxide Nanostructures for Advanced Electrocatalysis. *Chem. - A Eur. J.* **26**, 3943–3960. <https://doi.org/10.1002/chem.201903206>.
- Luo, X. F., Wang, J., Liang, Z. S., Chen, S. Z., Liu, Z. L., and C. W. Xu (2017). Manganese oxide with different morphology as efficient electrocatalyst for oxygen evolution reaction. *Int. J. Hydrogen Energy* **42**, 7151–7157. <https://doi.org/10.1016/j.ijhydene.2016.04.162>.
- El-Deab, M. S., Awad, M. I., Mohammad, A. M., and T. Ohsaka (2007). Enhanced water electrolysis: Electrocatalytic generation of oxygen gas at manganese oxide nanorods modified electrodes. *Electrochim. Commun.* **9**, 2082–2087. <https://doi.org/10.1016/j.elecom.2007.06.011>.
- Kesavan, G., and M. Chen (2021). Highly sensitive manganese oxide/hexagonal boron nitride nanocomposite: An efficient electrocatalyst for the detection of anti-cancer drug flutamide. *Microchem. J.* **163**, 105906. <https://doi.org/10.1016/j.microc.2020.105906>.
- Zheng, M., Zhang, H., Gong, X., Xu, R., Xiao, Y., Dong, H., Liu, X., and Y. Liu (2013). A simple additive-free approach for the synthesis of uniform manganese monoxide nanorods with large specific surface area. *Nanoscale Res. Lett.* **8**, 1–7. <https://doi.org/10.1186/1556-276X-8-166>.
- Kung, C. W., Lin, C. Y., Lai, Y. H., Vittal, R., and C. Ho (2011). Cobalt oxide acicular nanorods with high sensitivity for the non-enzymatic detection of glucose. *Biosens. Bioelectron.* **27**, 125–131. <https://doi.org/10.1016/j.bios.2011.06.033>.
- Wang, T., Xi, L., and J. Wang (2018). In situ fabrication of cobalt nanoflowers on sulfonated and fluorinated poly (arylene ether ketone-benzimidazole) template film for the electrocatalytic oxidation of glucose. *Talanta* **178**, 481–490. <https://doi.org/10.1016/j.talanta.2017.08.034>.
- Han, D., Ji, Y., Gu, F., and Z. Wang (2018). Cobalt oxide nanorods with special pore structure for enhanced ethanol sensing performance. *J. Colloid Interface Sci.* **531**, 320–330. <https://doi.org/10.1016/j.jcis.2018.07.064>.
- Mehrabi, A., Rahimnejad, M., Mohammadi, M., and Pourali (2019). Electrochemical detection of flutamide with gold electrode as an anticancer drug. *Biocatal. Agric. Biotechnol.* **22**, 101375. <https://doi.org/10.1016/j.biocab.2019.101375>.
- Tseng, T. W., Rajaji, U., Chen, T. W., Chen, S. M., Chen, Y. C., Huang, V., Mani, A., and A. Irudaya Jothi (2020). Sonochemical synthesis and fabrication of perovskite type calcium titanate interfacial nanostructure supported on graphene oxide sheets as a highly efficient electrocatalyst for electrochemical detection of chemotherapeutic drug. *Ultrason. Sonochem.* **69**, 105242. <https://doi.org/10.1016/j.ultsonch.2020.105242>.
- Ibrahim, H., and Y. Temerk (2020). A novel disposable electrochemical sensor based on modifying graphite pencil lead electrode surface with nanoacetylene black for simultaneous determination of antiandrogens flutamide and cyproterone acetate. *J. Electroanal. Chem.* **859**, 113836. <https://doi.org/10.1016/j.jelechem.2020.113836>.
- Ensafi, A. A., Talkhooncheh, B. M., Zandi-Atashbar, N., and Rezaei, B. (2020). Electrochemical Sensing of Flutamide Contained in Plasma and Urine Matrices Using NiFe<sub>2</sub>O<sub>4</sub>/rGO Nanocomposite, as an Efficient and Selective Electrocatalyst. *Electroanalysis* **32**, 1717–1724. <https://doi.org/10.1002/elan.202000048>.

27. Simple Sonochemical Synthesis of Cupric Oxide Sphere Decorated Reduced Graphene Oxide Composite for the Electrochemical Detection of Flutamide Drug in Biological Samples, (2022) 561902.
28. E Švorc, K. Borovská, K. Cinková, D. M. Stanković, and A. Planková (2017). Advanced electrochemical platform for determination of cytostatic drug flutamide in various matrices using a boron-doped diamond electrode. *Electrochim. Acta.* **251**, 621–630. <https://doi.org/10.1016/j.electacta.2017.08.077>.
29. N. Manjula, V. Vinothkumar, and S. M. Chen (2021). Synthesis and characterization of iron-cobalt oxide/polypyrrole nanocomposite: An electrochemical sensing platform of anti-prostate cancer drug flutamide in human urine and serum samples. *Colloids Surfaces A Physicochem. Eng. Asp.* **628**, 127367. <https://doi.org/10.1016/j.colsurfa.2021.127367>.
30. C. Saka (2019). Electroanalytical Approaches for Determination of Prostate Cancer Drugs in Biological Samples and Dosage Forms. *Crit. Rev. Anal. Chem.* **49**, 403–414. <https://doi.org/10.1080/10408347.2018.1538768>.
31. F. Ahmadi, J. B. Raoof, R. Ojani, M. Baghayeri, M. M. Lakouraj, and H. Tashakkorian (2015). Synthesis of Ag nanoparticles for the electrochemical detection of anticancer drug flutamide, Cuihua Xuebao/Chinese. *J. Catal.* **36**, 439–445. [https://doi.org/10.1016/S1872-2067\(14\)60209-6](https://doi.org/10.1016/S1872-2067(14)60209-6).
32. J. S. Farias, H. Zanin, A. S. Caldas, C. Costa, D. O. S. Santos, S. S. Luz, F. S. Damos, and R. D. E. Ca (2017). *Functionalized Multiwalled Carbon Nanotube Electrochemical Sensor for Determination of Anticancer Drug Flutamide* **46**, 5619–5628. <https://doi.org/10.1007/s11664-017-5630-6>.
33. N. M. Umesh, J. Antolin Jesila, S. F. Wang, M. Govindasamy, R. A. Alshgari, M. Ouladsmane, and I. V. Asharani (2021). Fabrication of highly sensitive anticancer drug sensor based on heterostructured ZnO-Co3O4 capped on carbon nitride nano-materials. *Microchem. J.* **167**, 106244. <https://doi.org/10.1016/j.microc.2021.106244>.
34. D. Balram, K. Y. Lian, N. Sebastian, and N. Rasana (2021). Ultrasensitive detection of cytotoxic food preservative tert-butylhydroquinone using 3D cupric oxide nanoflowers embedded functionalized carbon nanotubes. *J. Hazard. Mater.* **406**, 124792. <https://doi.org/10.1016/j.jhazmat.2020.124792>.
35. P. K. Brahman, L. Suresh, K. R. Reddy, and J. S. Bondili (2017). An electrochemical sensing platform for trace recognition and detection of an anti-prostate cancer drug flutamide in biological samples. *RSC Adv.* **7**, 37898–37907. <https://doi.org/10.1039/c7ra04243d>.
36. A. Rahi, K. Karimian, and H. Heli (2016). Nanostructured materials in electroanalysis of pharmaceuticals. *Anal. Biochem.* **497**, 39–47. <https://doi.org/10.1016/j.ab.2015.12.018>.
37. E. Asadian, M. Ghalkhani, and S. Shahrokhian (2019). Electrochemical sensing based on carbon nanoparticles: A review. *Sensors Actuators, B Chem.* **293**, 183–209. <https://doi.org/10.1016/j.snb.2019.04.075>.
38. C. M. Maroneze, A. Rahim, N. Fattori, L. P. Da Costa, F. A. Sigoli, I. O. Mazali, R. Custodio, and Y. Gushikem (2014). Electroactive Properties of 1-propyl-3-methylimidazolium Ionic Liquid Covalently Bonded on Mesoporous Silica Surface: Development of an Electrochemical Sensor Probed for NADH, Dopamine and Uric Acid Detection. *Electrochim. Acta.* **123**, 435–440. <https://doi.org/10.1016/j.electacta.2014.01.071>.
39. S. Tajik, H. Beitollahi, F. Garkani Nejad, I. Sheikhsaoie, A. S. Nugraha, H. W. Jang, Y. Yamauchi, and M. Shokouhimehr (2021). Performance of metal-organic frameworks in the electrochemical sensing of environmental pollutants. *J. Mater. Chem. A.* **9**, 8195–8220. <https://doi.org/10.1039/d0ta08344e>.
40. L. Liu, J.-f Song, Y. Peng-fei, and B. Cui (2006). A novel electrochemical sensing system for inosine and its application for inosine determination in pharmaceuticals and human serum. *Electrochim. Commun.* **8**, 1521–1526. <https://doi.org/10.1016/j.elecom.2006.07.013>.
41. M. Afzali, A. Mostafavi, and T. Shamspur (2020). Square wave voltammetric determination of anticancer drug flutamide using carbon paste electrode modified by CuO/GO/PANI nanocomposite. *Arab. J. Chem.* **13**, 3255–3265. <https://doi.org/10.1016/j.arabjc.2018.11.001>.
42. K. Venkatesh, B. Muthukutty, S. M. Chen, C. Karuppiah, B. Amanulla, C. C. Yang, and S. K. Ramaraj (2021). Nanomolar level detection of non-steroidal antiandrogen drug flutamide based on ZnMn<sub>2</sub>O<sub>4</sub> nanoparticles decorated porous reduced graphene oxide nanocomposite electrode. *J. Hazard. Mater.* **405**, 124096. <https://doi.org/10.1016/j.jhazmat.2020.124096>.
43. T. S. K. Sharma and K. Y. Hwa (2021). Rational design and preparation of copper vanadate anchored on sulfur doped reduced graphene oxide nanocomposite for electrochemical sensing of antiandrogen drug nilutamide using flexible electrodes. *J. Hazard. Mater.* **410**, 124659. <https://doi.org/10.1016/j.jhazmat.2020.124659>.
44. S. Ren, R. Feng, S. Cheng, L. Huang, Q. Wang, and Z. Zheng (2022). Construction of a sensitive electrochemical sensor based on hybrid 1 T/2H MoS<sub>2</sub> nanoflowers anchoring on rGO nanosheets for the voltammetric determination of acetaminophen. *Microchem. J.* **175**, 107129. <https://doi.org/10.1016/j.microc.2021.107129>.
45. F. Zhao, Y. Bai, L. Cao, G. Han, C. Fang, S. Wei, and Z. Chen (2020). New electrochemical DNA sensor based on nanoflowers of Cu<sub>3</sub>(PO<sub>4</sub>)<sub>2</sub>-BSA-GO for hepatitis B virus DNA detection. *J. Electroanal. Chem.* **867**, 114184. <https://doi.org/10.1016/j.jelecchem.2020.114184>.
46. Y. Wang, Y. Liang, S. Zhang, T. Wang, X. Zhuang, C. Tian, F. Luan, S. Q. Ni, and X. Fu (2021). Enhanced electrochemical sensor based on gold nanoparticles and MoS<sub>2</sub> nanoflowers decorated ionic liquid-functionalized graphene for sensitive detection of bisphenol A in environmental water. *Microchem. J.* **161**, 105769. <https://doi.org/10.1016/j.microc.2020.105769>.
47. K. J. Arun, A. K. Batra, A. Krishna, K. Bhat, M. D. Aggarwal, and P. J. Joseph Francis (2015). Surfactant Free Hydrothermal Synthesis of Copper Oxide Nanoparticles. *Am. J. Mater. Sci.* **5**, 36–38. <https://doi.org/10.5923/s.materials.201502.06>.
48. S.A. Moon, B.K. Salunke, B. Alkotaini, E. Sathiyamoorthi, plant extract Biological synthesis of manganese dioxide nanoparticles by Kalopanax pictus plant extract, (2015). <https://doi.org/10.1049/iet-nbt.2014.0051>.
49. V. Seshan, On the preparation , structural and magnetic properties of ZnO : Co nanoparticles On the preparation , structural and magnetic properties of ZnO : Co nanoparticles, (2014). <https://doi.org/10.1051/epjap/2014130316>.
50. N. Naveen, Investigation on physicochemical properties of Mn substituted spinel cobalt oxide for supercapacitor applications, (2019). <https://doi.org/10.1016/j.electacta.2014.01.161>
51. H. Yadegari, H. Wang, Three-dimensional MnO<sub>2</sub> ultrathin nanosheet aerogels for high- performance Li-O<sub>2</sub> batteries, (2015). <https://doi.org/10.1039/C5TA00004A>.
52. S.A. Moon, B.K. Salunke, P. Saha, A.R. Deshmukh, B.S. Kim, Comparison of dye degradation potential of biosynthesized copper oxide , manganese dioxide , and silver nanoparticles using Kalopanax pictus plant extract Comparison of dye degradation potential of biosynthesized copper oxide , manganese dioxide , and sil, (2018). <https://doi.org/10.1007/s11814-017-0318-4>.
53. V.A. Online, L.M. Alrehaily, J.M. Joseph, M.C. Biesinger, D.A. Guzonas, J.C. Wren, nanoparticle formation, (2013) 1014–1024. <https://doi.org/10.1039/c2cp43094k>.
54. Z. Liu, Controlled synthesis and characterization of layered manganese oxide nanostructures with different morphologies

- Controlled synthesis and characterization of layered manganese oxide nanostructures with different morphologies, (2014). <https://doi.org/10.1007/s11051-008-9517-6>.
55. V.A. Online, L. Yu, J. Zhu, J. Zhao, assembled by ultrathin nanoplates with enhanced supercapacitive performance †, (2014) 9353–9360. <https://doi.org/10.1039/c4ta00155a>.
56. Y. Khan, S.K. Durrani, M. Mehmood, M.R. Khan, I. Introduction, Mild hydrothermal synthesis of c-MnO<sub>2</sub> nanostructures and their phase transformation to a-MnO<sub>2</sub> nanowires, (2011). <https://doi.org/10.1557/jmr.2011.138>.
57. S. Barthwal and S. Lim (2019). Fabrication of long-term stable superoleophobic surface based on copper oxide / cobalt oxide with micro-nanoscale hierarchical roughness Applied Surface Science Fabrication of long-term stable superoleophobic surface based on copper oxide / cobalt oxide w. *Appl. Surf. Sci.* **328**, 296–305. <https://doi.org/10.1016/j.apsusc.2014.11.182>.
58. B. Mansouri, A. Maleki, S.A. Johari, Effects of cobalt oxide nanoparticles and cobalt ions on gill histopathology of zebrafish (*Danio rerio*), (2015).
59. S.P. Biosensor, S. Saeed, M. Rafiq, Q. Baloach, S. Habib, A. Naqvi, A. Tahira, H. Khain, A.A. Hullio, A.B. Mallah, Vanillin Assisted Synthesis of Co<sub>3</sub>O<sub>4</sub> Nanostructures for the Development of Vanillin Assisted Synthesis of Co<sub>3</sub>O<sub>4</sub> Nanostructures for the Development of Sensitive and Selective Peptone Biosensor, (2017). <https://doi.org/10.1166/sl.2017.3850>.
60. Y. Mi, X. Zhang, Z. Yang, Y. Li, S. Zhou, H. Zhang, W. Zhu, D. He, J. Wang, and G. Van Tendeloo (2007). Shape selective growth of single crystalline MnOOH multipods and 1D nanowires by a reductive hydrothermal method. *Mater. Lett.* **61**, 1781–1784. <https://doi.org/10.1016/j.matlet.2006.07.130>.
61. L. Shao, Q. Zhao, and J. Chen (2017). MnOOH nanorods as high-performance anodes for sodium ion batteries. *Chem. Commun.* **53**, 2435–2438. <https://doi.org/10.1039/c7cc00087a>.
62. A. Q. Mugheri, A. Tahira, S. T. H. Sirajuddin, M. . I. Sherazi, M. Abro, and Z. . H. . I. Willander (2016). An amperometric indirect determination of heavy metal ions through inhibition of glucose oxidase immobilized on cobalt oxide nanostructures. *Sens. Lett.* **14**, 1178–1186. <https://doi.org/10.1166/sl.2016.3752>.
63. P. Kar, F. Tatard, G. Lamblin, P. Banet, P. H. Aubert, C. Plesse, and C. Chevrot (2013). Silver nanoparticles to improve electron transfer at interfaces of gold electrodes modified by biotin or avidin. *J. Electroanal. Chem.* **692**, 17–25. <https://doi.org/10.1016/j.jelechem.2012.12.020>.
64. K. Edward Sekhosana, R. Nkhahle, and T. Nyokong (2020). Analytical Detection and Electrocatalysis of Paracetamol in Aqueous Media Using Rare-Earth Double-Decker Phthalocyanato Chelates as Electrochemically Active Materials. *ChemistrySelect*. **5**, 9857–9865. <https://doi.org/10.1002/slct.202002268>.
65. S. Manavalan, U. Rajaji, S. M. Chen, S. SteplinPaulSelvin, M. Govindasamy, T. W. Chen, M. AjmalAli, F. M. A. Al-Hemaid, and M. S. Elshikh (2018). Determination of 8-hydroxy-2'-deoxyguanosine oxidative stress biomarker using dysprosium oxide nanoparticles@reduced graphene oxide. *Inorg. Chem. Front.* **5**, 2885–2892. <https://doi.org/10.1039/c8qi00727f>.
66. R. Nkhahle, K. E. Sekhosana, S. Centane, and T. Nyokong (2019). Electrocatalytic Activity of Asymmetrical Cobalt Phthalocyanines in the Presence of N Doped Graphene Quantum Dots: The Push-pull Effects of Substituents. *Electroanalysis*. **31**, 891–904. <https://doi.org/10.1002/elan.201800837>.
67. K. E. Sekhosana, M. Shumba, and T. Nyokong (2019). Electrochemical Detection of 4-Chlorophenol Using Glassy Carbon Electrodes Modified with Thulium Double-Decker Phthalocyanine Salts. *ChemistrySelect*. **4**, 8434–8443. <https://doi.org/10.1002/slct.201803891>.
68. R. Karthik, M. Govindasamy, S. M. Chen, T. W. Chen, J. Vinoth Kumar, A. Elangovan, V. Muthuraj, and M. C. Yu (2017). A facile graphene oxide based sensor for electrochemical detection of prostate anti-cancer (anti-testosterone) drug flutamide in biological samples. *RSC Adv.* **7**, 25702–25709. <https://doi.org/10.1039/c6ra28792a>.
69. W. J. Lin, C. S. Liao, J. H. Jhang, and Y. C. Tsai (2009). Graphene modified basal and edge plane pyrolytic graphite electrodes for electrocatalytic oxidation of hydrogen peroxide and β-nicotinamide adenine dinucleotide. *Electrochim. Commun.* **11**, 2153–2156. <https://doi.org/10.1016/j.elecom.2009.09.018>.
70. T. Kokulnathan, R. Vishnuraj, T. J. Wang, E. A. Kumar, and B. Pullithadathil (2021). Heterostructured bismuth oxide/hexagonal-boron nitride nanocomposite: A disposable electrochemical sensor for detection of flutamide. *Ecotoxicol. Environ. Saf.* **207**, 111276. <https://doi.org/10.1016/j.ecoenv.2020.111276>.
71. T. Trinadh, H. Khuntia, T. Anusha, K. S. Bhavani, J. V. S. Kumar, and P. K. Brahman (2020). Synthesis and characterization of nanocomposite material based on graphene quantum dots and lanthanum doped zirconia nanoparticles: An electrochemical sensing application towards flutamide in urine samples. *Diam. Relat. Mater.* **110**, 108143. <https://doi.org/10.1016/j.diamond.2020.108143>.
72. M. Akilarasan, S. Maheshwaran, T. W. Chen, S. M. Chen, E. Tamilalagan, M. Ajmal Ali, W. A. Al-onazi, and A. M. Al-Mohaiomed (2020). Using cerium (III) orthovanadate as an efficient catalyst for the electrochemical sensing of anti-prostate cancer drug (flutamide) in biological fluids. *Microchem. J.* **159**, 105509. <https://doi.org/10.1016/j.microc.2020.105509>.
73. U. J. Pandit, I. Khan, S. Wankar, K. K. Raj, and S. N. Limaye (2015). Development of an electrochemical method for the determination of bicalutamide at the SWCNT/CPE in pharmaceutical preparations and human biological fluids. *Anal. Methods*. **7**, 10192–10198. <https://doi.org/10.1039/c5ay02025e>.
74. S. Kogularasu, M. Akilarasan, S. M. Chen, and J. K. Sheu (2021). Scalable and sustainable synthetic assessment between solid-state metathesis and sonochemically derived electrocatalysts (strontium molybdate) for the precise anti-androgen bicalutamide (Casodex™) detection. *Microchem. J.* **168**, 106465. <https://doi.org/10.1016/j.microc.2021.106465>.
75. A.S. Agnihotri, A. Varghese, N. M, Transition metal oxides in electrochemical and bio sensing: A state-of-art review, *Appl. Surf. Sci. Adv.* **4** (2021). <https://doi.org/10.1016/j.apsadv.2021.100072>

**Publisher's Note** Springer Nature remains neutral with regard to jurisdictional claims in published maps and institutional affiliations.